ARTICLE

# Mapping Localized Surface Plasmons within Silver Nanocubes Using Cathodoluminescence Hyperspectral Imaging

Paul R. Edwards,*,[†] David Sleith,[‡] Alastair W. Wark,[‡] and Robert W. Martin[†]

[†]Department of Physics, SUPA, University of Strathclyde, 107 Rottenrow, Glasgow G4 0NG, U.K.

[‡]Centre for Molecular Nanometrology, WestCHEM, Department of Pure and Applied Chemistry, University of Strathclyde, 295 Cathedral Street, Glasgow G1 1XL, U.K.

ABSTRACT: Localized surface plasmons within silver nanocubes less than 50 nm in size were investigated using high-resolution cathodoluminescence hyperspectral imaging. Multivariate statistical analysis of the multidimensional luminescence data set allows both the identification of distinct spectral features in the emission and the mapping of their spatial distribution. These results show a 490-nm peak emitted from the cube faces, with shorter-wavelength luminescence coming from the vertices and edges; this provides direct experimental confirmation of theoretical predictions.
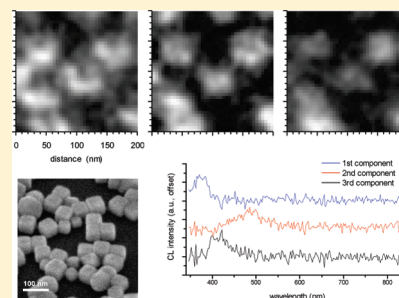
1. INTRODUCTION

The phenomenon of localized surface plasmon resonance (LSPR) results in significantly enhanced electric field intensities at the surfaces of metal nanoparticles in a dielectric medium. Based on the potential of these materials to enable the manipulation and focusing of light with nanoscale precision, a large range of possible applications are starting to emerge. These extend from high-density optical data recording,[1] metamaterial creation,[2] and nanoscale waveguides[3] to the design of new plasmon-enhanced spectroscopies for highly sensitive biomolecular sensing.[4,5]

Essential to advancing the field of nanoplasmonics is the development of experimental approaches that facilitate the understanding of electromagnetic interactions with metallic nanostructures. The small scale of such nanoparticles makes direct imaging of the electric field distribution particularly problematic, with feature sizes well beneath the diffraction limit encountered by standard optical techniques. Photon−plasmon coupling is the most common mechanism for studying plasmons, with the physical dimensions of each confocal[6] or near-field[7] optically imaged nanostructure having to be determined independently using atomic force or electron microscopy techniques. However, surface plasmons can also be generated by the interaction of an electron beam with the metal/dielectric surface.[8] Recent work utilizing a scanning transmission electron microscope equipped to perform electron energy-loss spectroscopy (EELS) has enabled the profiling of surface plasmons with ∼1-nm spatial resolution as demonstrated with silver nanotriangles[9] and coupled spherical[10] and nanorod dimers.[11]

Cathodoluminescence (CL) imaging, whereby the energy transferred from incident electrons to the plasmonic structure is observed through subsequently emitted photons, provides information complementary to that obtained from EELS. CL imaging can be carried out in a suitably modified scanning or transmission electron microscope and generally takes the form of a combination of monochromatic imaging (in which the intensity within a given band of wavelengths is mapped) and spectroscopy (in which the luminescence spectrum is measured at selected fixed points). Electric field distributions in gold[12] and silver[13] nanorods on the scale of hundreds of nanometers have previously been mapped using this approach, as have silver nanoparticles with dimensions of ∼100 nm or greater.[14,15]

However, a potentially more powerful variant of the CL technique is that of hyperspectral imaging.[16] In this mode, a luminescence spectrum is acquired at each spatial position as the electron beam scans an area of the sample, resulting in a data cube containing the full set of spectrally and spatially resolved information. Later analysis can be used to extract, for example, simple monochromatic images and single-point spectra, but unlike the more basic types of CL measurement, it also allows shifts in emission energy to be mapped. Additionally, the multidimensional nature of the data also lends itself to analysis using powerful multivariate statistical methods. Bashevoy et al.[17] demonstrated the use of such hyperspectral CL in the imaging of surface plasmon polariton modes in a 590-nm-long Au nanoresonator.

In this work, we applied hyperspectral CL imaging to much smaller (<50-nm) nanoparticles for the first time. The inherently low intensity associated with LSPR emission in single nanoparticles of this size has until now prevented it from being sufficiently resolved both spectrally and spatially while maintaining a usable

signal-to-noise ratio. Because of the high magnification necessary to observe the particles, the sensitivity of the technique to image drift of only a few nanometers precludes the simple adoption of long acquisition times to overcome the signal problem. Instead, we have applied a number of advances to overcome this limitation. First, the development of an optimized directly coupled optical imaging system to collect the CL allows the emission to be spectrally resolved without a drop in signal throughput. Second, a recently developed high-sensitivity, low-noise sensor was used for the light detection. Finally, we employed a data treatment that exploits the multivariate nature of the hyperspectral CL data set.

Individual silver nanocubes were studied that, when compared with spheres, exhibit more than one simple dipole resonance and have a shape that is more amenable to controlled self-assembly.[18] Furthermore, because the local electric fields at the edges and corners are predicted to be relatively greater,[19] characterization of such structures is an important step in the long-term goal of creating more complex plasmonic devices.

2. EXPERIMENTAL SECTION

2.1. Nanocube Preparation. Ag nanocubes were prepared by the sulfide-mediated polyol method established by the Xia group.[20,21] In summary, 6 mL of ethylene glycol (Sigma, ≥99.5%) was added to a 24 mL reaction vial and heated in an oil bath at 150 °C for 1 h with the vial cap loosely closed. The reaction solution was continuously stirred using a magnetic stir bar. A number of solutions were freshly prepared using ethylene glycol (EG)/poly-(vinylpyrrolidone) (PVP; $M_r \approx 55000$, Sigma) at 20 mg/mL, $AgNO_3$ (>99.9%, Sigma) at a concentration of 48 mg/mL, and 3 mM $Na_2S.9H_2O$ (Sigma). Following the 1-h preheating of EG, the fresh Na_2S solution was agitated using a vortex mixer, and 90 μL was transferred to the reaction vials. The vial cap was replaced loosely, and approximately 9 min was allowed to elapse before addition of 1.5 mL of the PVP solution in two 0.75 mL aliquots, followed immediately by 0.5 mL of the $AgNO_3$ solution. The caps were again loosely replaced on the vials, and the reaction was continued for a further 15 min or so until the medium turned a dark green accompanied by a red-tinted meniscus. Following quenching of the reaction by placing the vial in a water bath at room temperature, the reaction mixture was cleaned by adding ~50 mL of acetone and centrifuging at 2000g for 30 min. The supernatant was removed, and the pellet of cubes was redispersed in distilled water. This was centrifuged again at 9000g for 10 min, the supernatant was discarded, and the process was repeated a further two times. The final product was redispersed and stored in Milli-Q water for further use.

2.2. Scanning Electron Microscopy (SEM) Measurement. The cube samples were prepared for SEM and CL analysis by dropping ~10 μL of the stock solution onto a clean Si wafer substrate and allowing it to air-dry. Cathodoluminescence measurements were carried out in an FEI Sirion 200 field-emission SEM instrument using the custom-built CL system outlined in Figure 1. The silicon substrate supporting the nanoparticles was inclined at a 45° angle with respect to the electron beam. The emitted luminescence was collected and collimated using a Schwarzschild-type reflecting objective with a numerical aperture of 0.28 that was oriented with its optical axis perpendicular to the beam. The collimated light was brought to an $f/\#$-matched focus at the 100-μm entrance slit of a $^1/_8$-m spectrograph using an off-axis paraboloidal mirror and detected using an Andor-cooled
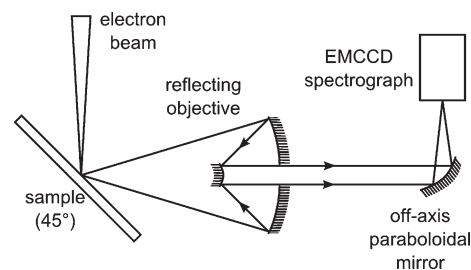

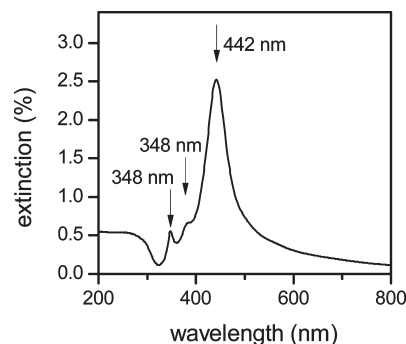**Figure 1.** System used for cathodoluminescence hyperspectral imaging.

Figure 2. UV/visible extinction spectrum of the Ag nanocubes in aqueous suspension.
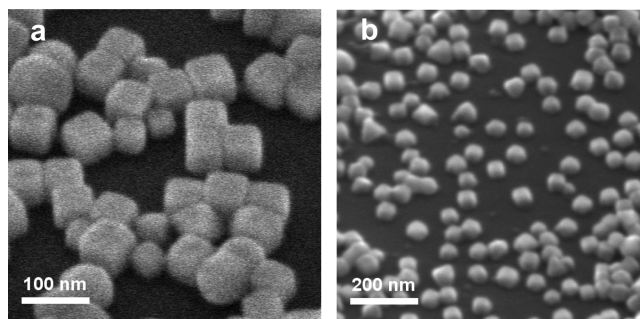

Figure 3. (a) High-resolution and (b) high-beam-power secondary electron images of different regions of the sample.

electron-multiplying charge-coupled device (EMCCD). On-chip full vertical binning was applied to the 1600 × 200 pixel array, and 4× horizontal binning resulted in 400 spectral channels. Hyperspectral images were obtained by recording a spectrum at each pixel while scanning the electron beam, with an exposure time of 40 ms per spectrum.

3. RESULTS AND DISCUSSION

Figure 2 shows the measured UV/visible extinction spectrum of the nanocubes in an aqueous environment, which exhibits a dominant peak at 442 nm that can be attributed to a dipole resonance excitation. This is not significantly different from the results of Sherry et al.[20] and Skrabalak et al.,[21] who measured peaks at 444 and ~450 nm, respectively, for mean side lengths of 30 and 45 nm. The shorter-wavelength feature at 348 nm and the shoulder at 376 nm might result from a quadrupole contribution[18] or from resonances in noncubic nanoparticles in the suspension.
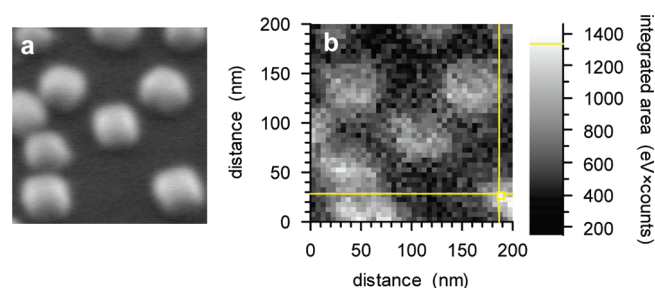
Figure 4. (a) Magnified central portion of SEM image with (b) corresponding panchromatic CL map.
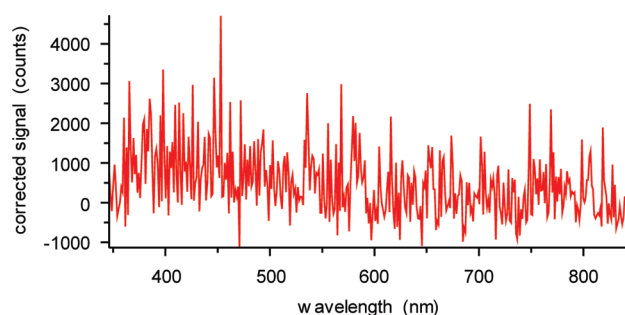

Figure 5. One constituent spectrum from the CL hyperspectral image, corresponding to the position shown in Figure 4b.

Figure 6. Scree plot showing eigenvalues corresponding to the first eight principal components of the hyperspectral CL image.

An SEM secondary electron micrograph of the nanocubes is shown in Figure 3, which was obtained using a low-power (5 kV, 20 pA) beam in order to ensure optimum resolution. Measuring the dimensions of around 100 cubes yielded an edge length distribution of 48 ± 8 nm, with about 80−90% of the sample composed of cubes and the remainder consisting of a mixture of spheres, bipyramids, and rods. The beam was then set to a significantly higher power (30 kV, 40 nA) to excite cathodoluminescence at a detectable intensity, with the resultant larger spot size limiting the spatial resolution of subsequent images.

A CL hyperspectral image of the central 200 × 200 nm portion of the latter field of view was acquired, using a step size of 5 nm. Integrating each spectrum in the data set over the full wavelength range yielded the CL intensity image seen in Figure 4. This is equivalent to an image acquired by a conventional CL system operating in panchromatic mode and shows a clear correlation between the location of the nanocubes and the emission of CL.

A spectrum from the hyperspectral image, corresponding to the pixel marked with a crosshair in Figure 4b, is reproduced in Figure 5. Despite representing one of the highest-intensity pixels in the data set, the low overall signal level results in even this spectrum being dominated by noise. Such a low signal-to-noise ratio would make conventional monochromatic CL imaging extremely challenging. The signal level is also too low to benefit from nonlinear least-squares curve fitting (e.g., of a Gaussian peak), as previously applied to such hyperspectral image data.[22]

However, a significant advantage of recording the CL in hyperspectral imaging mode is the ability to extract distinct spectral and spatial features from the data cube using multivariate statistical analysis techniques. Such techniques have been applied to various multidimensional microscopy results, including X-ray microanalysis,[23] transmission electron microscopy,[24] and more
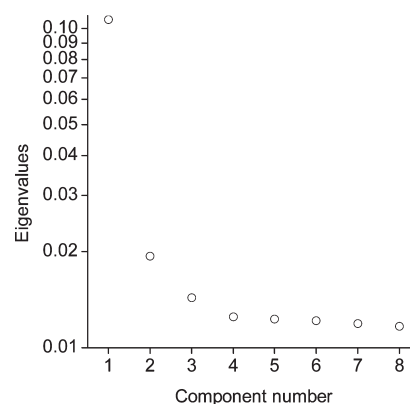
recently CL.[25,17] One such technique, principal component analysis (PCA), allows the most significant underlying variables of a multidimensional data set to be identified. In the case of hyperspectral images, this results in each spectrum being described no longer as a sum of discrete monochromatic wavelengths but instead as a linear combination of (still orthogonal) unit vectors in variable space, known as scores or "eigenspectra". The eigenvalues emerging from this analysis represent the fraction of the data's total variance that is explained by that component, allowing the most significant components to be retained and the less significant, noise-dominated ones to be discarded. In matrix form, this can described by

$$\mathbf{X}[n,m] \, = \, \mathbf{W}[n,r]\mathbf{H}[r,m] \, + \, \mathbf{R} \approx \mathbf{WH}$$

where $\mathbf{X}[n,m]$ is the mean-adjusted data cube containing n spectral channels and m spatial positions; $\mathbf{W}[n,r]$ contains the first r eigenspectra (where $r \leq n$); and $\mathbf{H}[r,m]$ is the array of loadings, or the relative contribution of each eigenspectrum to the spectrum at each spatial position. $\mathbf{R}$ represents the residual resulting from the discarded $(n - r)$ components, which reduces to zero as r approaches n.

A varimax orthogonal rotation is generally then applied to the few retained components; this maximizes the sum of the variance of the components at each wavelength, thus minimizing any overlap between the spectra and simplifying interpretation. The resultant rotated spectra $\mathbf{V}[n,r]$ can then be used as basis functions for extracting two-dimensional spatial images (loadings) $\mathbf{L}[r,m]$ from the hyperspectral image. Because $\mathbf{V}$ remains orthogonal, this is simply done using

$$\mathbf{V}^{\mathrm{T}}\mathbf{X} = \mathbf{V}^{\mathrm{T}}\mathbf{VL} = \mathbf{L}$$

PCA was carried out on the CL hyperspectral image using the nonlinear iterative partial least-squares (NIPALS) method. The associated eigenvalues (the first eight of which are shown in the "scree" plot in Figure 6) indicate that the first three PCA components are the most significant, responsible (before rotation) for ∼10.7%, 1.9%, and 1.4%, respectively, of the variance of the data set. We therefore considered the effects of retaining the first one, two, or three components in our analysis.

The first eigenspectrum and its corresponding image are shown in Figure 7. This shows the dominant spectral shape of the data set; however, despite explaining the highest fraction by far of the data variance compared with lesser components, it gives little extra insight into the luminescence. In effect, the spectrum
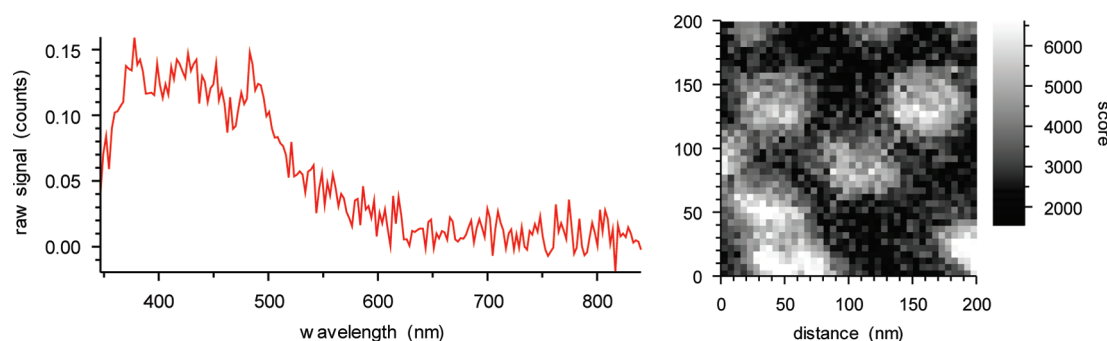
Figure 7. (Left) Spectrum and (right) image for the first principal component.
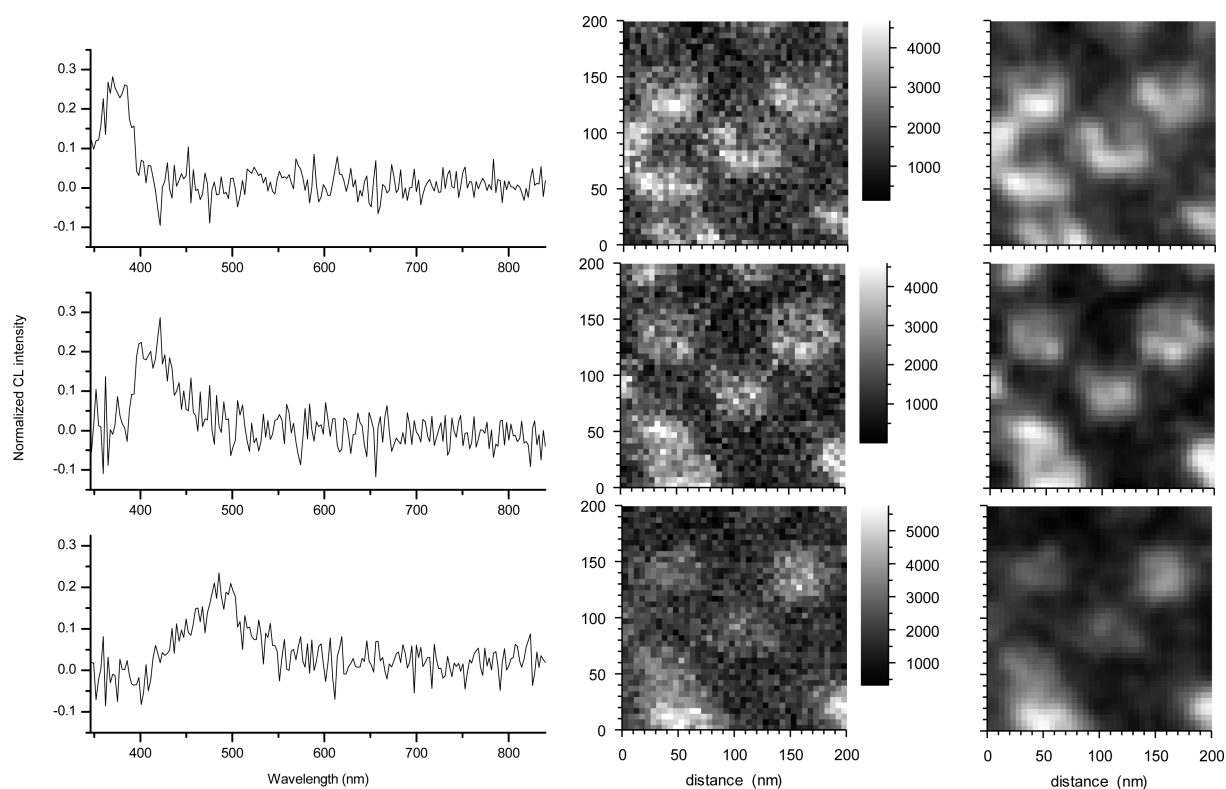

Figure 8. (Left) Spectra and (center) images obtained by retaining the first three principal components, along with (right) the results of wavelet filtering of the images to reduce spatial noise.

represents a mean spectrum from the nanocubes, and the image gives no more information than the panchromatic image in Figure 4b.

If instead the first two components are retained and a varimax rotation is applied, the first component shows a peak at around 380 nm, and the second shows a double peak at ∼420 and 490 nm (not shown). The corresponding images show the shorter-wavelength emission to be localized at the edges/corners of the cubes, with the longer-wavelength luminescence appearing to come more from the nanoparticle centers. The apparent double peak in the second spectrum and the fact that the third eigenvalue is still notably higher than the subsequent components suggest that the third eigenspectrum should also be included in the analysis. The results of this analysis are reproduced in Figure 8 and do indeed show all three peaks to be separated into separate components. The narrow 380-nm peak

still correlates strongly with the edges and corners, with less intense emission collected from the top edges. This latter effect is due to the 45° sample tilt used during the CL imaging, suggesting that the emission is directional. The 420-nm component appears partially localized to these same edge regions, whereas the 490-nm peak is associated with the cube centers.

As a guide to the eye, noise-filtered images are also shown (Figure 8, right); these were generated by removing the higher-frequency (noisier) spatial components using Haar wavelet decomposition. These results can be compared with the finite-difference time-domain (FDTD) modeling of similar Ag nanocubes by Sherry et al.[20] (in this case, on a glass rather than Si substrate), which predicted the appearance of a narrow peak at a shorter wavelength than that of the dominant dipole excitation, with emission localized at those vertices not adjacent to the substrate. The presence of this peak is due to each cube effectively

experiencing two different dielectric environments: that of the medium and that of the substrate. We interpret the 490- and 420-nm peaks seen in our results as corresponding to the dipole excitation (red-shifted from the 442 nm seen in Figure 2 due to the different dielectric environment) and the substrate-related peak, respectively. The 380-nm peak, which is strongly associated with the cube edges/vertices, has not previously been reported. This might be the result of an additional dipole resonance associated with these regions of the cube, distinct from the main dipole peak; García de Abajo[26] provided a semianalytical treatment of such dipole resonances in spherical nanoparticles. This work is the first direct confirmation of the localization of specific emission peaks at the vertices for nanocubes of this scale.

A number of factors have been reported to cause LSPR emission peaks to shift in wavelength, including proximity of the cube to the substrate,[20] cube size,[18] and corner sharpness.[27] This offers a possible explanation for the 380-nm peak emerging from the PCA: Rather than being distinct spectral features, the first and second spectra in Figure 8 might instead represent a single peak with varying wavelength. Other factors, including cross-talk between the more closely spaced nanocubes, could also contribute to variation in the emission wavelength.

CONCLUSIONS

By combining careful optical design, high-sensitivity detection, and multivariate statistical analysis, we have shown that hyperspectral CL imaging is capable of mapping localized surface plasmons in nanostructures with a spatial resolution approaching ~10 nm. Using this method, we achieved sufficient spatial resolution to probe plasmon modes in ~50-nm silver nanocubes for the first time and to identify emission peaks specifically associated with the cube edges and vertices.

AUTHOR INFORMATION

Corresponding Author
*E-mail: paul.edwards@strath.ac.uk.

ACKNOWLEDGMENT

REFERENCES

(1) Zijlstra, P.; Chon, J. W. N.; Gu, M. *Nature* **2009**, *459*, 410–413.

(2) Pendry, J. B.; Schurig, D.; Smith, D. R. *Science* **2006**, *312*, 1780–1782.

(3) Lal, S.; Link, S.; Halas, N. J. *Nat. Photonics* **2007**, *1*, 641–648.

(4) Sannomiya, T.; Hafner, C.; Voro, J. *Nano Lett.* **2008**, *8*, 3450–3455.

(5) Graham, D.; Thompson, D. G.; Smith, W. E.; Faulds, K. *Nat. Nanotechnol.* **2008**, *3*, 548–551.

(6) Hu, M.; Novo, C.; Funston, A.; Wang, H.; Staleva, H.; Zou, S.; Mulvaney, P.; Xia, Y.; Hartland, G. V. *J. Mater. Chem.* **2008**, *18*, 1949–1960.

(7) Rang, M.; Jones, A. C.; Zhou, F.; Li, Z.-Y.; Wiley, B. J.; Xia, Y.; Raschke, M. B. *Nano Lett.* **2008**, *8*, 3357–3363.

(8) Ritchie, R. H.; Ashley, J. C.; Emerson, L. C. *Phys. Rev.* **1964**, *135*, A759–A763.

(9) Nelayah, J.; Kociak, M.; Stephan, O.; García de Abajo, F. J.; Tence, M.; Henrard, L.; Taverna, D.; Pastoriza-Santos, I.; Liz-Marzan, L. M.; Colliex, C. *Nat. Phys.* **2007**, *3*, 348–353.

(10) Koh, A. L.; Bao, K.; Khan, I.; Smith, W. E.; Kothleitner, G.; Nordlander, P.; Maier, S. A.; McComb, D. W. *ACS Nano* **2009**, *3*, 3015–3022.

(11) Chu, M. W.; Myroshnychenko, V.; Chen, C. H.; Deng, J. P.; Mou, C. Y.; García de Abajo, F. J. *Nano Lett.* **2009**, *9*, 399–404.

(12) Vesseur, E. J. R.; de Waele, R.; Kuttge, M.; Polman, A. *Nano Lett.* **2007**, *7*, 2843–2846.

(13) Gómez-Medina, R.; Yamamoto, N.; Nakano, M.; García de Abajo, F. J. *New J. Phys.* **2008**, *10*, 105009.

(14) Chaturvedi, P.; Hsu, K. H.; Kumar, A.; Fung, K. H.; Mabon, J. C.; Fang, N. X. *ACS Nano* **2009**, *3*, 2965–2974.

(15) Yamamoto, N.; Araya, K.; García de Abajo, F. J. *Phys Rev. B* **2001**, *64*, 205419.

(16) Martin, R. W.; Edwards, P. R.; O'Donnell, K. P.; Dawson, M. D.; Jeon, C. W; Liu, C.; Rice, G. R.; Watson, I. M. *Phys. Status Solidi A-Appl. Mat.* **2004**, *201*, 665–672.

(17) Bashevoy, M. V.; Jonsson, F.; MacDonald, K. F.; Chen, Y.; Zheludev, N. I. *Opt. Express* **2007**, *15*, 11313–11320.

(18) Zhou, F.; Li, Z.-Y.; Liu, Y.; Xia, Y. *J. Phys. Chem. C* **2008**, *112*, 20233–20240.

(19) Rycenga, M.; McLellan, J. M.; Xia, Y. *Adv. Mater.* **2008**, *20*, 2416–2420.

(20) Sherry, L. J.; Chang, S.-H.; Schatz, G. C.; Van Duyne, R. P.; Wiley, B. J.; Xia, Y. *Nano Lett.* **2005**, *5*, 2034–2038.

(21) Skrabalak, S. E.; Au, L.; Li, X.; Xia, Y. *Nat. Protoc.* **2007**, *2*, 2182.

(22) Edwards, P. R.; Martin, R. W.; Watson, I. M.; Liu, C.; Taylor, R. A.; Rice, J. H.; Na, J. H.; Robinson, J. W.; Smith, J. D. *Appl. Phys. Lett.* **2004**, *85*, 4281–4283.

(23) Kotula, P. G.; Keenan, M. R.; Michael, J. R. *Microsc. Microanal.* **2003**, *9*, 1–17.

(24) Bonnet, N. *J. Microsc.* **1998**, *190*, 2–18.

(25) Edwards, P. R.; Martin, R. W.; Lee, M. R. *Am. Mineral.* **2007**, *92*, 235–242.

(26) García de Abajo, F. J. *Rev. Mod. Phys* **2010**, *82*, 209–275.

(27) McMahon, J, M.; Wang, Y.; Sherry, L. J.; Van Duyne, R. P.; Marks, L. D.; Gray, S. K.; Schatz, G. C. *J. Phys. Chem. C* **2009**, *113*, 2731–2735.